nature communications

Article

https://doi.org/10.1038/s41467-026-74996-9

Controllable patterning of magnetic bits with atomically sharp boundaries

Received: 10 November 2025

Accepted: 17 June 2026

Published online: 23 July 2026

Check for updates

Qi Wang[1,2,3], Lei Jin[4], Dongsheng He[5], Hideto Yanagihara[6,7,8], Eiji Kita[6], Rafal E. Dunin-Borkowski[4], Fu-Rong Chen[1,2,3] & Xiaoyan Zhong[1,2,3]

Magnetic information bits in magnetic media are approaching their fundamental thermodynamic limits, creating an urgent need for high-precision nanoscale fabrication methods. Here we establish a proof-of-concept demonstration for fabricating, controlling, and testing closely spaced individual magnetic bits at the nanometre scale. An aberration-corrected atomic-sized electron probe directly sculpts ferrimagnetic (FM) spinel $NiFe_2O_4$ bits within an antiferromagnetic (AFM) rock-salt spacer by beam-induced phase transition. Through in situ nanobeam electron magnetic circular dichroism (EMCD), which probes the out-of-plane magnetization component, we perform single-domain magnetometry. This demonstrates detectable magnetic signals from a domain with a lateral width of ~4 nm, thermodynamically supported by the surrounding AFM matrix via exchange bias coupling. Furthermore, we achieve the deterministic writing of binary information ("1" and "0") by reversing the localized magnetization direction of individual FM bits under an applied external magnetic field. By establishing a complete, closed-loop workflow from atomic-scale fabrication to single-bit magnetic readout, this study demonstrates a pathway toward engineering future high-density magnetic architectures.

The explosive growth of data-intensive applications like artificial intelligence and cloud computing is creating an unprecedented demand for higher-density data storage[1,2]. This demand is pushing magnetic data storage towards its fundamental thermodynamic barrier[3–6]. This continuous scaling relies on the creation of physically-isolated, deep-nanoscale magnetic domains—serving as individual magnetic information bits—to carry data[7–9]. However, as the dimensions of these functional magnetic bits shrink into the sub-10 nm regime, realizing stable arrays faces two formidable physical bottlenecks. First, fabricating magnetic bits with deep-nanoscale (sub-10 nm) precision remains a formidable barrier[7], a major obstacle is creating arrays of sub-10 nm islands with the required uniformity and line-edge roughness, which pushes beyond the limits of conventional lithography[10,11]. Conventional techniques, such as directed self-assembly and advanced lithography, struggle with severe line-edge roughness (~2–5 nm) and uniformity issues, failing to define precise bit boundaries at these dimensions. Second, and more fundamentally, scaling bits below 10 nm triggers the superparamagnetic effect[12]. As the bit volume (V) shrinks, the thermal stability factor ($\Delta = K_u V / k_B T$) decreases drastically, leading to spontaneous magnetization reversal at room temperature[13,14]. For instance, in $MnFe_2O_4$ nanoparticles synthesized from reverse micelles, the saturation magnetization

[1]TRACE EM Unit, Department of Materials Science and Engineering and Hong Kong Institute for Clean Energy (HKICE), City University of Hong Kong, Hong Kong SAR, PR China. [2]City University of Hong Kong Matter Science Research Institute (Futian Shenzhen), Shenzhen, PR China. [3]Nanomanufacturing Laboratory (NML), City University of Hong Kong Shenzhen Research Institute, Shenzhen, PR China. [4]Ernst Ruska-Centre for Microscopy and Spectroscopy with Electrons, Forschungszentrum Jülich GmbH, Jülich, Germany. [5]Core Research Facilities, Southern University of Science and Technology, Shenzhen, PR China. [6]Department of Applied Physics, University of Tsukuba, Tsukuba, Japan. [7]Tsukuba Research Center for Energy Materials Science (TREMS), University of Tsukuba, Tsukuba, Japan. [8]Tsukuba Research Center for Organic-Inorganic Quantum Spin Science and Technology (OIQSST), University of Tsukuba, Tsukuba, Japan. e-mail: xzhong25@cityu.edu.hk

decreases from approximately 73 emu/g at 13.5 nm to 35 emu/g at 4.4 nm[14]. Interfacial exchange bias—achieved by magnetically coupling a ferromagnetic (FM) bit with an antiferromagnetic (AFM) matrix—has emerged as a highly effective strategy to provide additional pinning anisotropy and enhance the effective reversal barrier[15,16].

Translating this physical concept into reality necessitates an advanced methodology capable of both patterning sub-5 nm bits with atomic precision and simultaneously verifying their magnetic reliability. Emerging atomic-scale tools[17], such as scanning tunneling microscopy[18–21] and atomic force microscopy[22], excel at manipulating weakly bonded surface atoms but are inadequate for the three-dimensional solid-state reconfiguration required for robust magnetic devices. Furthermore, conventional magnetic probes, such as magnetic force microscopy or tunneling magnetoresistance sensors, lack the sub-10 nm spatial resolution to measure an individual bit's magnetic state while correlating it to its local atomic structure[23]. A more versatile platform is the focused electron beam of a scanning transmission electron microscopy (STEM)[17], which has been adapted from pure imaging to an "atomic forge" capable of site-specific transformations inside solids—including phase engineering, controlled creation/migration of vacancies and lattice impurities, beam-driven reduction and epitaxial crystallization in complex oxides, and atomic-scale reconstructions at oxide interfaces—thereby enabling direct fabrication of electronic and magnetic functionalities[24–27]. Simultaneously, when coupled with advanced analytical techniques—such as electron magnetic circular dichroism (EMCD)[28] for extracting element-specific out-of-plane magnetization, and differential phase contrast (DPC)[29] imaging for mapping local electromagnetic fields—STEM uniquely enables the direct probing of magnetic states at the exact same spatial coordinates. Utilizing this dual capability to both create and verify sub-5 nm magnetic domains with atomic precision offers a compelling pathway to address the scaling bottlenecks of magnetic nanostructures.

In this work, we present an integrated proof-of-concept demonstration for patterning, controlling, and verifying deep-nanoscale magnetic information bits. We employ a focused aberration-corrected electron probe not merely as an imaging tool, but as a direct-fabrication tool. This is achieved by locally inducing a phase transition that converts the native ferrimagnetic (FM) spinel $NiFe_2O_4$ into an antiferromagnetic (AFM) rock-salt structure. Consequently, this process sculpts a 1D cross-sectional array prototype of isolated bits with lateral widths down to ~4 nm, perfectly embedded within a magnetically active AFM matrix. This configuration creates atomically sharp FM/AFM interfaces that minimize line-edge roughness for precise bit isolation. Furthermore, the interfacial coupling supplies extra pinning anisotropy, enhancing magnetic stability and pushing the superparamagnetic threshold to smaller bit sizes. The direct-patterning process is governed by a quantitative, real-time feedback loop based on live analysis of atomic column intensities, enabling deterministic control of bit size with atomic precision. Significantly, in situ nanobeam EMCD provides single-bit magnetometry, experimentally confirming the detectable out-of-plane magnetic signal from these ~4 nm isolated bits, whose thermal stability is inherently supported by the engineered FM/AFM interfacial exchange coupling. By establishing a closed-loop workflow from atomic-precision fabrication to nanoscale magnetic validation, this work provides a fundamental physical blueprint for engineering future high-density magnetic architectures.

Results

The conceptual architecture and experimental realization of our site-specific nanoscale patterning approach are presented in Fig. 1. Our design employed a Cs-corrected electron probe as a direct-pattern tool to locally convert regions of a FM film into an AFM matrix. This process allows us to precisely define individual magnetic bits that are not just physically isolated, but also magnetically coupled to the surrounding AFM matrix (Fig. 1a). This coupling is intentionally designed to generate exchange bias, a phenomenon that can enhance the thermal stability of the FM bits[15]. Fig. 1b provides direct, atomic-resolution HAADF-STEM validation of this strategy, showing a successfully fabricated 1D cross-sectional array prototype in a pristine $NiFe_2O_4/MgAl_2O_4$ film (Supplementary Fig. 1a) in which FM spinel bits—the functional information bits—are separated by an AFM rock-salt matrix that serves as an isolating spacer. The process allows for full, precise control over the patterned architecture, as both the size of the bits and their inter-bit spacing are readily tunable by manipulating the scan parameters of the electron probe.

The structural basis for this function-defining transformation is revealed by atomic-resolution STEM imaging along the [110] zone axis. The pristine FM bit material, spinel $NiFe_2O_4$, shows site-specific cation ordering with distinct column types (Fig. 1c). The atomic-resolution images, together with the structural model, resolve tetrahedral Fe-only C-sites (red) and mixed Fe/Ni octahedral A- and B-sites (yellow) (as classified in Supplementary Fig. 1b, c). In ADF imaging, Z-contrast differentiates the cation columns (with A-sites showing higher projected intensity along [110] due to their two-fold projected density), while ABF imaging visualizes the light element oxygen sublattice, allowing the coordination cages to be identified. The combination of cation contrast and oxygen coordination thus distinguishes all three site types. This inverse-spinel cation arrangement produces a net ferrimagnetic moment through A–B sublattice imbalance[30]. Upon targeted electron irradiation, this structure is converted into the AFM spacer material, rock-salt $(Ni_{1/3}Fe_{2/3})O$, as shown in Fig. 1d. The clearest sign of this change is the complete disappearance of the tetrahedral Fe (C-site) columns together with the homogenization of octahedral sites. The resulting symmetric structure is antiferromagnetic, making it a perfect medium to both isolate and magnetically stabilize the FM bits. Crucially, this change in crystal structure is what defines the function of the material. By locally converting selected areas into the AFM matrix while preserving adjacent regions as FM islands, our patterning process simultaneously defines the bits and the active spacer in a single in situ step, without altering surface topography or requiring ex situ processing. This structural reconfiguration, confirmed by reciprocal space analysis (Supplementary Fig. 1d–f), is therefore the key mechanism enabling the single-step, in situ fabrication of these nanoscale magnetic architectures. Notably, the phase transition is thermodynamically irreversible under ambient conditions. To experimentally validate the long-term structural stability of the patterned regions, we re-examined the fabricated structures after 24 days of storage at room temperature. High-resolution STEM imaging confirmed that the engineered AFM rock-salt spacer and the atomically sharp FM/AFM interfaces remained perfectly intact, with no signs of spontaneous recovery back to the pristine spinel phase (Supplementary Fig. 1g). This robust environmental stability ensures the long-term reliability of the patterned discrete magnetic domains.

Having demonstrated the conceptual design to create these FM/AFM interfacial coupled magnetic bits, we then performed a detailed investigation to confirm their properties and understand the underlying physical mechanism during the transformation induced by the electron beam (Fig. 2). Paired HAADF-STEM images and measured projected charge-density maps (from 4D-STEM) of the pristine spinel phase and the converted rock-salt phase in the exact same region confirm the expected rearrangement of the atomic lattice (Fig. 2a, b). More specifically, line profiles extracted from the measured charge-density maps show a significant decrease at the oxygen-column, from ~2 e/Å^2 in the pristine structure to ~1 e/Å^2 after patterning (Fig. 2c, d), which we identify as the key experimental signature of oxygen loss. This assignment is directly corroborated by both differentiated differential phase contrast STEM (dDPC-STEM) simulations and integrated differential phase contrast STEM (iDPC-STEM) (Supplementary Fig. 2), which consistently demonstrate that the introduction of

https://doi.org/10.1038/s41467-026-74996-9

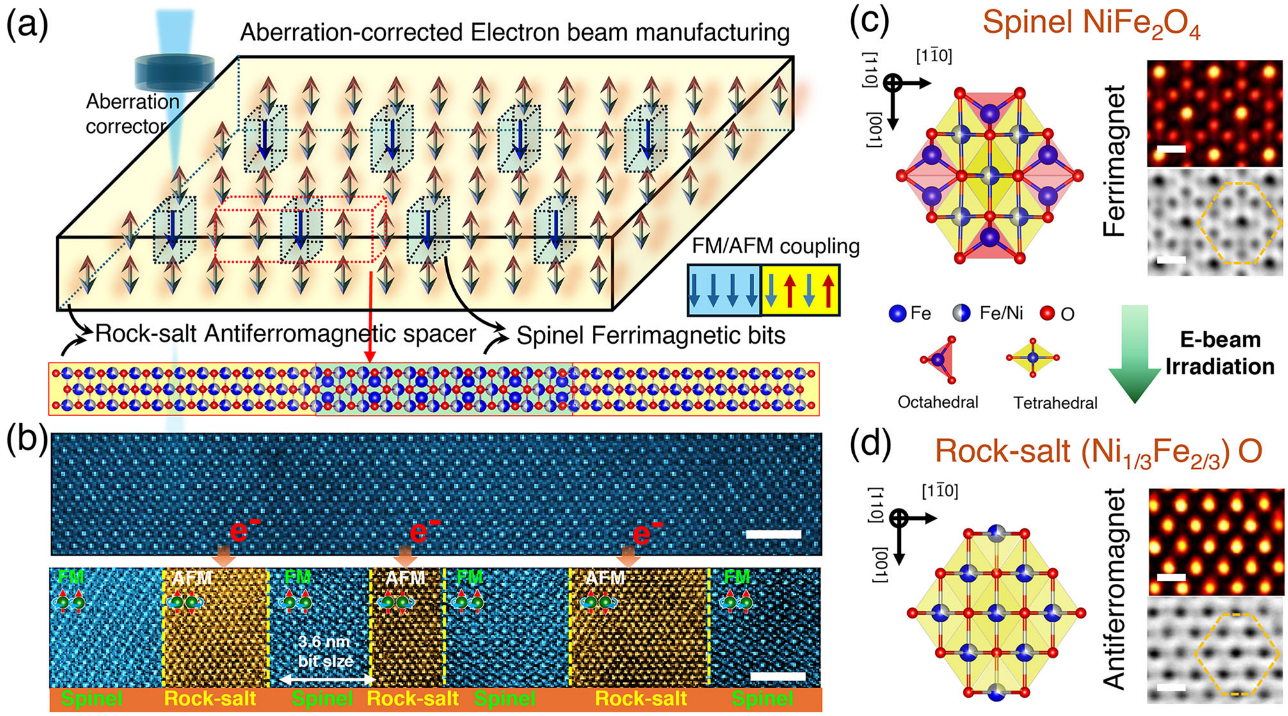

Fig. 1 | Conceptual architecture and experimental realization of an atomically fabricated magnetic bit. a Schematic diagram of the fabrication strategy. A focused electron beam is used as a direct-pattern tool to convert regions of a ferrimagnetic (FM) film into an antiferromagnetic (AFM) matrix, thereby defining and isolating individual magnetic information bits and the FM/AFM interface. The red frames depict the atomic model of a typical FM bit. **b** Atomic-resolution HAADF-STEM images of a pristine and a fabricated bit array, demonstrating the successful creation of FM spinel bits (the information carriers) separated by AFM rock-salt matrix (the isolating spacer). The size and inter-bit spacing (pitch) are tunable by manipulating the electron beam's scan parameters. Scale bar, 2 nm. **c** Atomic structure of the FM bit material, spinel $NiFe_2O_4$, viewed along the [110] zone axis. The imaging clearly distinguishes tetrahedral Fe-only sites (C-sites, modeled in red) and octahedral Fe/Ni sites (A- and B-sites, modeled in yellow). Scale bar, 0.25 nm. **d** Atomic structure of the AFM spacer material, rock-salt $(Ni_{1/3}Fe_{2/3})_3O_3$. Its simple, symmetric structure, containing only octahedral cation sites (yellow), gives rise to a compensated antiferromagnetic order, making it an ideal medium for magnetically decoupling the information bits. Note the complete disappearance of the tetrahedral Fe columns (red), a definitive fingerprint of the structural transformation. Scale bar, 0.25 nm.

oxygen vacancies into the structural model leads to a corresponding reduction of charge at the O columns. This oxygen removal is the expected result of a knock-on mechanism, in which the high-energy electron beam physically displaces oxygen atoms from the lattice[24,31,32], while the simultaneous increase in B-site column intensity yields an Fe/O charge density ratio evolving from ~1.15 to ~2.8 (Fig. 2c, d), indicating synchronous metal-site rearrangement. On the other hand, the oxygen framework remains largely unchanged—as evidenced by the consistent black frames in Fig. 2a, b—indicating that the phase transition is selective, preserving the oxygen sublattice topology while allowing metal-site rearrangement. In addition, time-resolved 4D-STEM analysis of the iDPC-STEM images and local electric field across initial, intermediate, and final states (Supplementary Fig. 3) shows that oxygen depletion accompanies the entire conversion pathway.

This structural transformation is accompanied by a corresponding change in the material's chemical composition. Atomic-resolution EDS mapping (Fig. 2e, f, Supplementary Fig. 4) reveals the fundamental cation distribution. In the pristine inverse spinel state (Fig. 2e), the maps confirm that tetrahedral sites are predominantly occupied by Fe (red), while octahedral sites are composed of a mixture of Fe and Ni (blue). After the transformation, the AFM spacer (Fig. 2f) exhibits a chemically homogeneous distribution consistent with a rock-salt framework. Time-resolved EDS mapping (Supplementary Fig. 4) vividly captures this redistribution of iron and nickel atoms during the process. Moreover, EDS measurement (Fig. 2g, Supplementary Fig. 5) provides quantitative confirmation of this oxygen loss, revealing a measured reduction in the oxygen-to-metal ratio from ~59 to ~51 at.%. We note that absolute EDS values under zone-axis conditions can be influenced by channeling effects; nevertheless, the downward trend is robust and is independently corroborated by the projected charge-density maps (Fig. 2a, b), which show reduced signal at oxygen-column positions. Importantly, despite this oxygen depletion, the oxygen sublattice maintains an approximately cubic framework throughout the transformation—as further evidenced by the consistent white frames in Fig. 2e, f, building on the unchanged oxygen sublattice frame marked by the black frames in Fig. 2a, b, and aligning with the topologies of both the spinel and the rock-salt phases.

These changes in structure and chemical composition directly impact the electronic states of the metal atoms, which in turn govern the material's magnetic function. To probe this crucial link, we used electron energy-loss spectroscopy (EELS) to investigate the valence states of the Fe and Ni atoms. Analysis of the O K-edge (Fig. 2h, Supplementary Fig. 6a) reveals a marked reduction in the intensity of the pre-peak feature (indicated by the black arrow) in the AFM spacer. This pre-peak, corresponding to transitions into unoccupied hybridized O *2p*–Fe *3d* states, reflects the effective Fe valence, and its suppression indicates electron filling[33,34]. This is further confirmed by the Fe L-edge analysis (Fig. 2i, Supplementary Fig. 6b, d). We observe a distinct chemical shift of the L_3 peak to lower energy (from 711.2 to 709.9 eV) and, critically, a significant decrease in the L_3/L_2 intensity ratio from 4.8 to 3.3. Both are well-established spectroscopic signatures for the reduction of iron's oxidation state from Fe^{3+} towards Fe^{2+}. In contrast, the Ni L-edge shows no clear energy shift and no systematic change in white-line ratio (Supplementary Fig. 6c), indicating that Ni remains essentially in the Ni^{2+} state across the conversion.

 https://doi.org/10.1038/s41467-026-74996-9

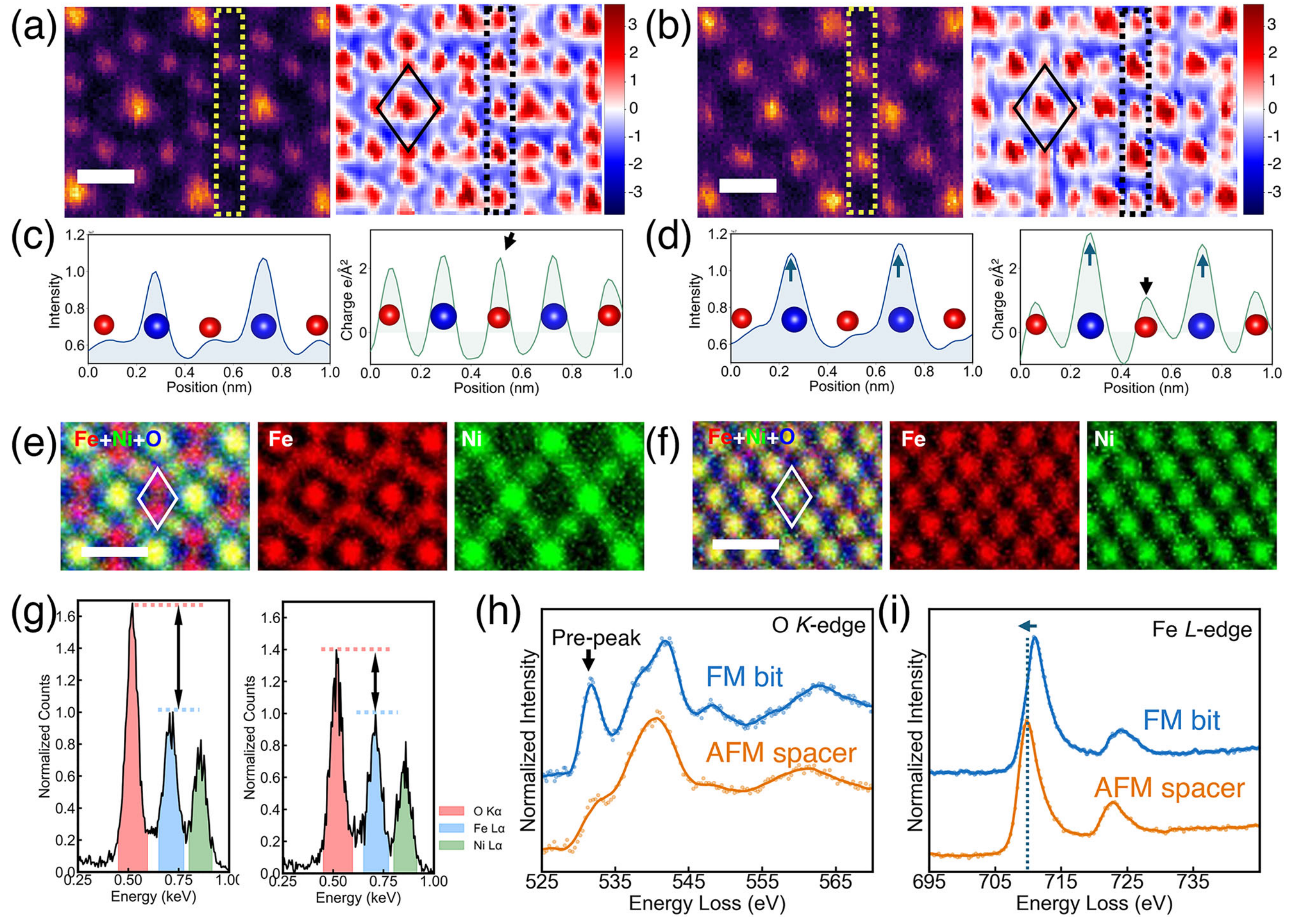

Fig. 2 | Elucidating the transformation mechanism between the FM bit and AFM spacer. HAADF-STEM images and projected charge density maps (from 4D-STEM) of the pristine spinel (FM) bit (**a**) and the final rock-salt (AFM) spacer (**b**). Scale bars, 0.25 nm. The black frames indicate the preservation of the oxygen sublattice frame. **c**, **d** Line profiles taken from the corresponding yellow and black boxes in (**a**, **b**). In the pristine state (**c**) the charge-density map reveals O and cation columns with comparable projected charge density, whereas in the final state (**d**) the oxygen column density is markedly reduced—providing direct evidence of oxygen loss—while the cation columns exhibit increased HAADF intensity and charge density, as indicated by the blue arrows. Atomic-resolution EDS elemental maps (Fe, red; Ni, blue; O, green) and separated Fe/Ni occupancy maps before (**e**) and after (**f**) the transformation. Scale bar, 0.5 nm. In the pristine spinel structure (**e**), tetrahedral sites are predominantly occupied by Fe, while octahedral sites host a mixture of Fe and Ni – consistent with the expected spinel cation ordering. In the rock-salt structure (**f**) Fe and Ni are uniformly distributed across octahedral sites, and tetrahedral sites vanish, as expected for the rock-salt topology; the oxygen sublattice retains an approximately cubic framework, as indicated by the white frame. **g** Fe-Lα–normalized EDS spectra implying that the transformation involves a net reduction in the oxygen-to-metal signal ratio. Core-loss EELS analysis of the **h** O *K*-edge and **i** Fe *L*-edge. The O *K*-edge spectrum (**h**) shows a marked reduction of the pre-peak (indicated by the black arrow), while the Fe *L*-edge spectrum (**i**) exhibits a chemical shift to lower energy (indicated by the blue arrow).

Taken together, these results support a coherent mechanism in which electron-beam knock-on sputtering removes lattice oxygen, creating oxygen vacancies that facilitate cation rearrangement. The associated decrease in the oxygen-to-metal ratio and the filling of Fe *3d*–O *2p* states reduce Fe^{3+} to Fe^{2+}, while the altered stoichiometry and coordination provide the thermodynamic drive for cooperative cation rearrangement into the stable rock-salt phase. This multi-modal evidence distinguishes the functional states of the FM bits and AFM spacers and anchors their single-step fabrication in a well-defined physical process.

The central objective of our fabrication process is to precisely control this phase transformation, enabling the creation of information bits with tailored sizes and atomically sharp interfaces—such that line-edge roughness remains sufficiently low. Achieving this level of deterministic control requires a robust, real-time monitoring and feedback system. We developed such a system by analyzing the STEM images as they are being acquired, creating a live "progress bar" for the structural transformation (Fig. 3). High-magnification image series, like the typical example in Fig. 3a, show the gradual evolution of the transformation, which completes over a practical timeframe of approximately 4 min under a total electron dose of ~1.6×10^4 $e^-/Å^2$ (Supplementary Movie 1). The core of our feedback loop is a real-time quantitative analysis of the atomic column intensities derived from each incoming HAADF-STEM frame (Fig. 3b–d; Supplementary Figs. 7 and 8). Taking advantage of the HAADF signal's sensitivity to the number and type of atoms in a column ($I \propto Z^{\alpha}N$)[35], we can track the evolution of the different cation site populations. Metal sites are classified by their projected lattice position into octahedral A- and B-sites and tetrahedral C-sites in the spinel phase, together with new octahedral D-sites that appear in the rock-salt phase (Supplementary Fig. 7b). This analysis yields a clear process indicator, in which the population of C-sites decreases while D-sites emerge, with corresponding shifts in the site intensity distributions (Fig. 3d). By monitoring the statistical distributions of these site intensities in real time (Fig. 3d), we obtain a precise measure of how complete the structural conversion is. This quantitative feedback allows us to stop the electron beam exposure at the exact moment the desired transformation is complete, thus preventing unwanted overexposure damage or incomplete fabrication.

https://doi.org/10.1038/s41467-026-74996-9

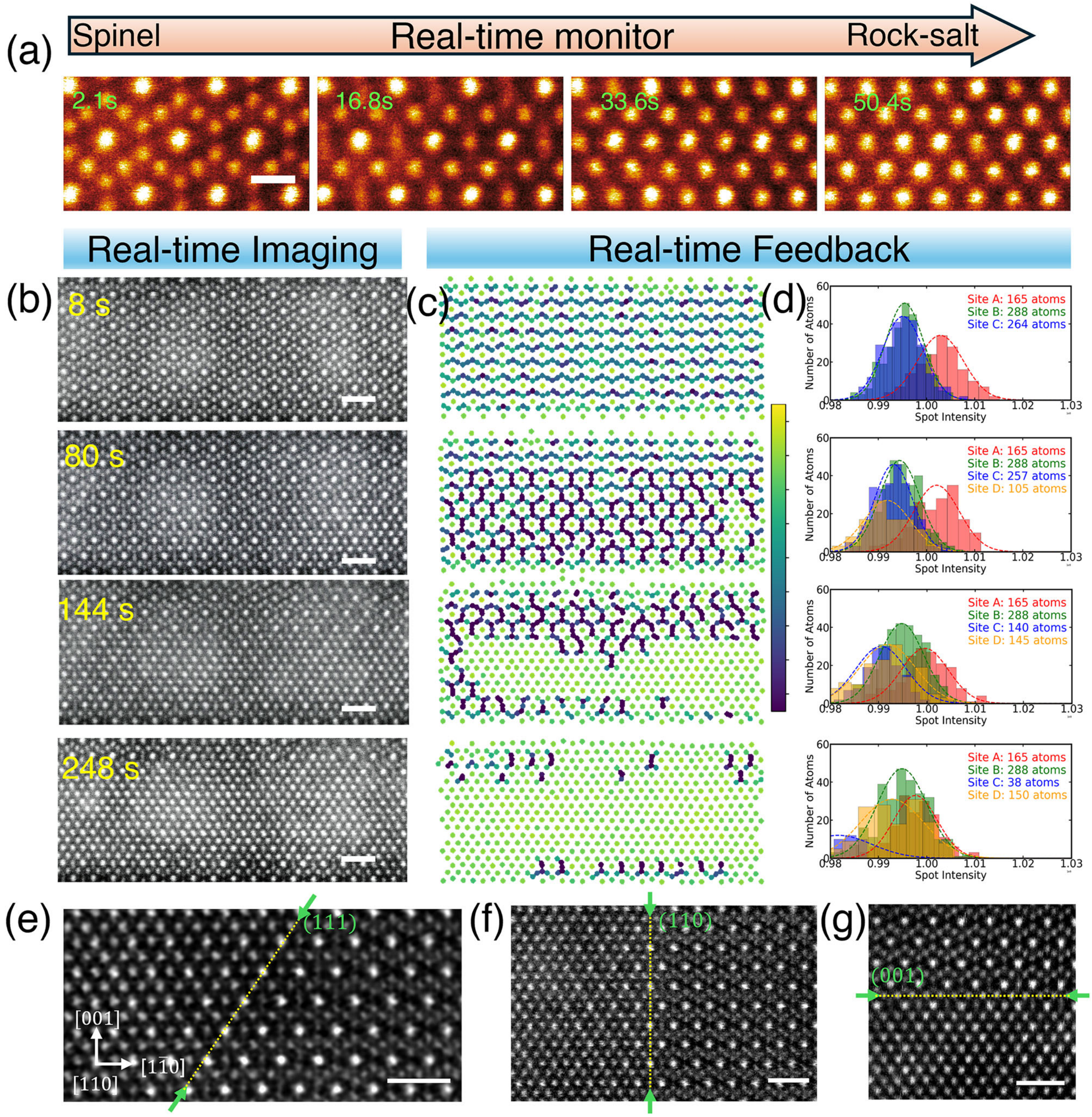

Fig. 3 | Real-time monitoring and control for atomic-scale interface engineering. a High-magnification, time-resolved atomic ADF images monitoring the atomic-level conversion from a FM bit to AFM spacer material. Scale bar, 0.5 nm. Live STEM imaging (**b**) is processed via real-time atomic intensity mapping (**c**) and statistical site intensity analysis (**d**) to provide a feedback signal for controlling the fabrication of magnetic bits. Scale bar, 1 nm. **e**–**g** High-fidelity engineering of atomically sharp interfaces between the FM bit and AFM spacer material, enabled by real-time feedback. By aligning the beam scan direction and region, interfaces along the **e** (111), **f** (110), and **g** (100) crystallographic planes were deterministically created. The dashed yellow lines and green arrows highlight the resulting interfaces. Scale bars, 1 nm.

ive analysis not only provides the quantitative feedback for precise process control but also gives direct insight into how the phase transition happens at the atomic scale. A clear three-step kinetic pathway can be resolved from the feedback loop. The transition is initiated by oxygen loss, which is evidenced by an immediate drop at the oxygen-column positions in the projected charge density profiles together with a concurrent decrease in the oxygen-to-metal ratio from EDS (Fig. 2c–g; Supplementary Fig. 5). In tandem, EELS data confirm the resulting Fe^{3+} to Fe^{2+} reduction through a diminished O K-edge pre-peak and a shifted Fe L-edge with a lower L_3/L_2 ratio (Fig. 2h, i). The new structure is then nucleated by C-site displacement, where the live column tracker shows tetrahedral Fe (C) columns fading as their positions migrate toward octahedral positions. This is accompanied by symmetry-sensitive changes in 4D-STEM Bragg disk intensities and a redistribution of projected electric field (Supplementary Fig. 3). Finally, the rearrangement of the A, B, and C sublattices completes the conversion, whereby the original octahedral Fe/Ni columns homogenize as A and B sites merge, C-sites vanish, and the new D-site population becomes dominant. Importantly, throughout all stages, the oxygen sublattice framework remains geometrically continuous, indicating that, while knock-on events remove oxygen locally, dynamical lateral migration and replenishment from adjacent regions help

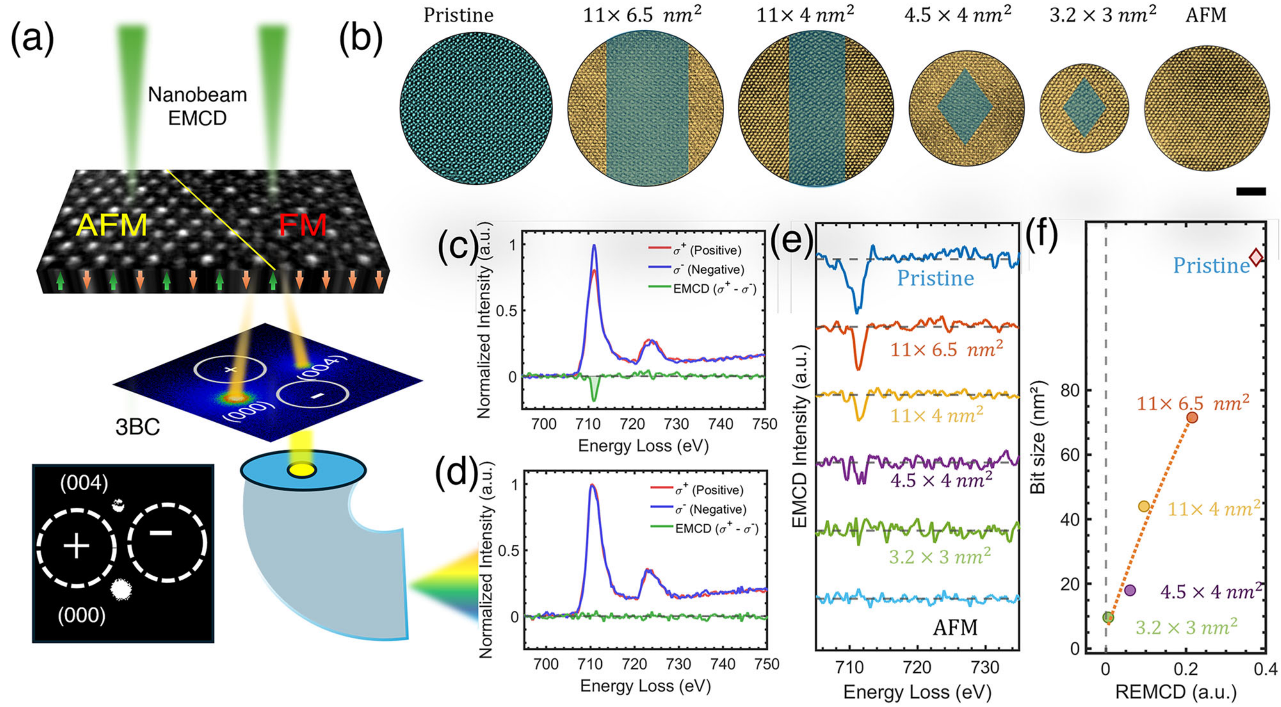

Fig. 4 | Probing size-dependent local magnetic states and determining the thermodynamic stability limit in deep-nanoscale domains. a Schematic diagram of the nanobeam EMCD technique used to probe the magnetic state of an individual magnetic bit. The nanobeam diffraction pattern shows the three-beam case (3BC) orientation, with the white circles representing the positions of the entrance aperture for positive (+) and negative (−) EELS collection. **b** Series of fabricated FM bits with systematically decreasing sizes. Scale bar, 2 nm. **c**, **d** EMCD measurements from the Fe L-edge under (004) 3BC conditions. A significant dichroic signal is measured from the FM $NiFe_2O_4$ bit with a size of $11 \times 6.5\ nm^2$ (**c**), while a null signal is obtained from the AFM rock-salt matrix (**d**). Red and blue lines are the raw EELS spectra from the "+" and "−" positions; the green line is the resulting EMCD signal. **e**, **f** Size-dependent magnetic performance of the fabricated bits. The EMCD signals (**e**) and the relative EMCD strength (REMCD) (**f**) decrease with bit size. The magnetic signal vanishes at a critical dimension of ~3.2 nm × 3 nm, providing a direct determination of the size limit of information bits with detectable magnetic signals.

maintain the framework. Operationally, these three physical milestones provide the "stop/go" cues for process control: oxygen decrease signals entry into the conversion window, C-site collapse marks nucleation, and A/B homogenization with D-site emergence sets the termination threshold that preserves atomically-sharp FM/AFM boundaries.

This real-time feedback gives extremely precise control over the final structure. As a definitive demonstration, we show that by simply programming the electron beam's scan direction relative to the crystal lattice, we can deterministically sculpt atomically sharp FM/AFM interfaces that minimize line-edge roughness. Figure 3e–g presents successful engineering of these interfaces along user-defined (111), (110), and (100) crystallographic planes. The ability to create custom, atomically sharp interfaces on-demand is a direct result of our live process control and represents a significant advance in atomic-precision materials engineering.

Following the deterministic fabrication of these 1D cross-sectional array prototypes enabled by real-time feedback control, we next verified the local magnetic states of the resulting information bits. To resolve the intrinsic magnetism at the deep-nanoscale, we employed nanobeam EMCD with a highly focused electron probe. Under our specific diffraction conditions, the probe size is precisely controlled at ~1.8 nm. This extreme spatial localization ensures that the magnetic signal is extracted exclusively from the irradiated sub-2 nm volume, providing a rigorous foundation for probing individual magnetic bits without spatial averaging. In the protocol, the sample was tilted to a three-beam configuration (3BC), exciting the (004) systematic reflection (Fig. 4a), and EELS spectra were acquired with entrance apertures placed at the chiral "+" and "−" scattering positions for individual bits. This technique provides a local magnetometric signal inherently aligned with the STEM image, ideal for resolving deep-nanoscale out-of-plane magnetic information. As internal reference, the pristine spinel $NiFe_2O_4$ yields a robust EMCD feature (Supplementary Fig. 9b), while the rock-salt spacer exhibits a null EMCD signal within the noise level (Fig. 4d). This confirms the expected ferrimagnetic and compensated antiferromagnetic states, respectively, and validates that our direct-pattern process successfully defines the intended magnetic phases. The EMCD feature is preserved after embedding the information bits within the AFM spacer, as evidenced by a representative $11.0 \times 6.5\ nm^2$ bit (Fig. 4c).

To probe the size-dependence of saturated magnetization, we fabricated an array of FM bits with progressively smaller dimensions (Fig. 4b; Supplementary Fig. 9a) and measured EMCD from each information bit under an external magnetic field of ~2.5 T. Figure 4e presents raw EMCD spectra of the Fe *L*-edge for five representative bits, with lateral dimensions spanning $11.0 \times 6.5\ nm^2$ down to $3.2 \times 3.0\ nm^2$. Figure 4f reveals the relative EMCD strength (REMCD) proportional to the local saturated magnetization of the five information bits under identical acquisition geometry and sample thickness. Supplementary Figs. 9 and 10 provide full Fe- and Ni-edge raw spectra across the size series, along with corresponding bit images, for independent assessment of signal-to-noise and spectral consistency. Specifically, as the dimensions shrink from $11.0 \times 6.5\ nm^2$ toward $4.5 \times 4.0\ nm^2$, the Fe *L*-edge EMCD signal weakens progressively (Fig. 4e, f). Bits at $3.2 \times 3.0\ nm^2$ yield no discernible EMCD feature, whereas those at $4.5 \times 4.0\ nm^2$ retain a magnetically-detectable signal. A similar trend holds for the Ni *L*-edge (Supplementary Fig. 8), despite higher noise. We therefore identify $4.5 \times 4.0\ nm^2$ as the detectable bit size in our architecture in terms of size-dependent saturated magnetization in superparamagnetism, which lies well below the typical size limit of ~10 nm expected for isolated magnetic nanoparticles of this

https://doi.org/10.1038/s41467-026-74996-9

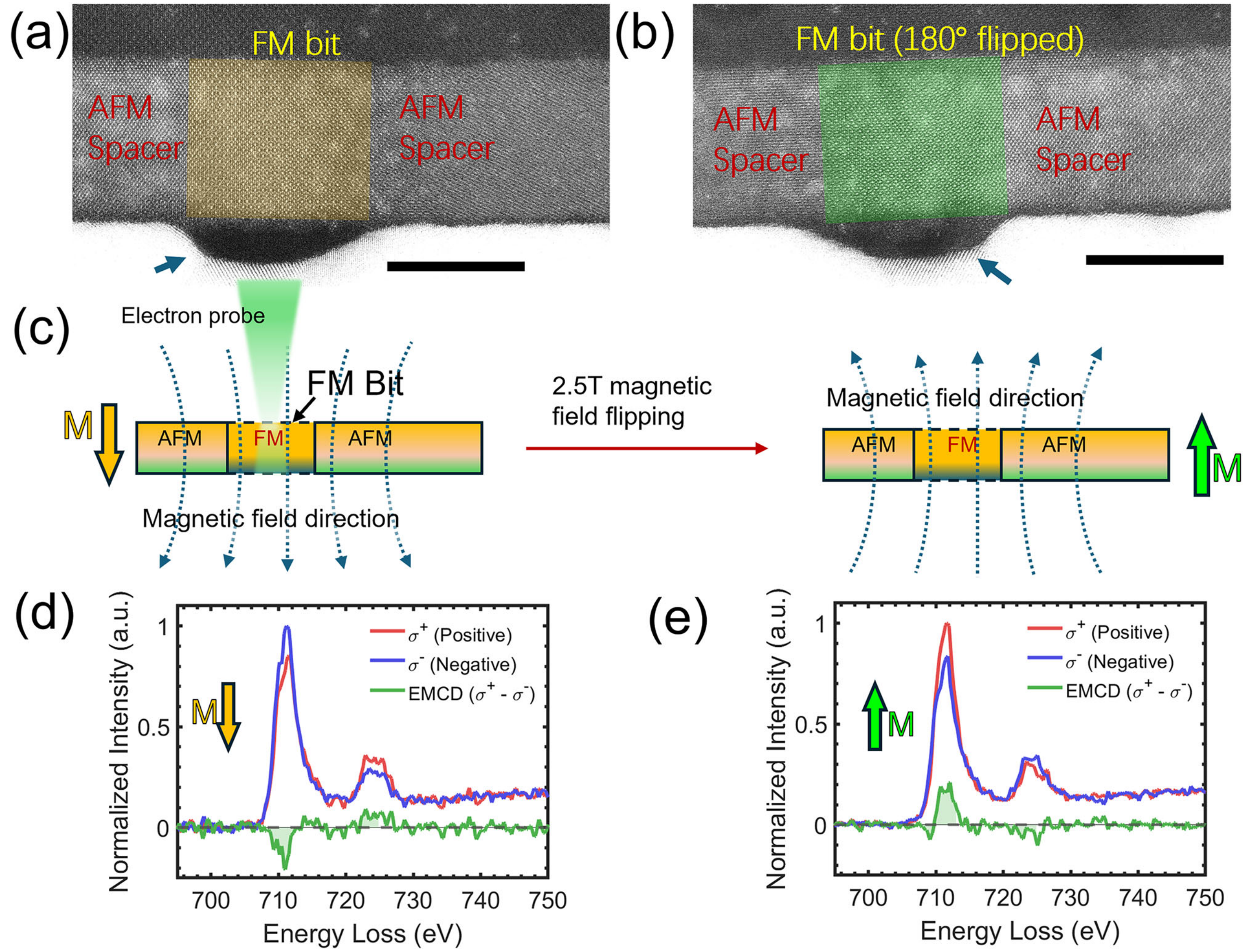

Fig. 5 | Proof-of-concept demonstration of binary information writing ("1" and "0") in an individual magnetic bit via magnetization reversal. Annular dark-field scanning transmission electron microscopy (ADF-STEM) images of the ferrimagnetic (FM) bit **a** before and **b** after a 180° physical sample inversion. The distinct geometric notch at the sample edge provides explicit visual confirmation of the spatial rotation. The localized magnetic states, which are directly validated by the reversed electron magnetic circular dichroism (EMCD) signals, are graphically encoded as binary information "1" (yellow overlay) and "0" (green overlay) on the individual FM bit. Scale bars, 10 nm. **c** Schematic illustration depicting the equivalence between applying an opposite external magnetic field and physically inverting the sample within the fixed magnetic environment of the transmission electron microscope (TEM). The ~1.8 nm focused electron probe in nanobeam EMCD mode is significantly smaller than the lateral dimensions of the discrete bits, enabling highly localized, bit-by-bit readout of intrinsic magnetic information. Corresponding nanobeam EMCD spectra acquired under identical parameters **d** before and **e** after flipping the sample upside down by 180°. The reversed EMCD signals of this FM magnetic bit before and after flipping confirm its reversed magnetization direction M marked by "1" with a yellow arrow and "0" with a green arrow when writing its information in opposite directions with a 2.5 T objective lens magnetic field applied.

type at room temperature[36,37]. To further validate the thermodynamic stability of these deep-nanoscale bits, complementary micromagnetic simulations were performed (Supplementary Fig. 11). The results explicitly demonstrate that FM bits embedded within an AFM matrix exhibit substantially broadened magnetic hysteresis loops (Supplementary Fig. 11b, c) and enhanced coercivity (H_c) at extreme downscaling (e.g., down to 3 nm) compared to isolated bits. Furthermore, the spatial distribution of magnetic vectors for an 11 nm bit visually corroborates this stabilization: while the embedded bit strictly maintains a highly-ordered single domain state (Supplementary Fig. 11e), the isolated bit degenerates into a randomized spin configuration (Supplementary Fig. 11f), characteristic of thermal instability. These theoretical findings perfectly bridge our experimental EMCD observations with the thermodynamic requirements for stable magnetic domains. Notably, we link structure and magnetism at the level of a single bit by recording EMCD spectra. Each data point links a specific atomic configuration (verified in Figs. 1–3 and Supplementary Figs. 4–8) to its magnetic readout, rather than being averaged over an ensemble. Within this framework, the size-dependent effect that we have measured directly reflects the physically embedded environment, including crucial interfacial exchange coupling, rather than an isolated particle.

To explicitly validate the deterministic writing of magnetic information, we performed a proof-of-concept demonstration of reversing the localized magnetization direction under an applied external magnetic field. By physically inverting the patterned specimen by 180°(Fig. 5a, b), the fixed ~2.5 T perpendicular magnetic field generated by the TEM objective lens is effectively applied anti-parallel to the original crystallographic surface normal along the optical z-axis. This spatial configuration is physically equivalent to subjecting the fixed magnetic bits to an opposite saturation magnetic field (Fig. 5c). Nanobeam EMCD spectra acquired before and after the sample inversion both exhibit the characteristic features of magnetic chiral dichroism originating from spin magnetic moments[38]. Crucially, the extracted EMCD signals at the L_3 and L_2 edges exhibit a complete polarity reversal upon inversion (Fig. 5d, e). According to the established EMCD sum rules, the integral of these spectra over the $L_{2,3}$ edges is strictly proportional to the projection and strength of the local

 https://doi.org/10.1038/s41467-026-74996-9

magnetization vector. Therefore, this pronounced signal reversal experimentally confirms the deterministic inversion of the magnetization direction (**M**). We graphically encode these reversed magnetic states as binary information, marking the opposite magnetization directions as "1" (indicated by the yellow arrow and spatial color contrast, Fig. 5a, d) and "0" (indicated by the green arrow and contrast, Fig. 5b, e). Furthermore, it is crucial to emphasize that this localized magnetic information is addressed bit-by-bit without any adjacent crosstalk. Because the ~1.8 nm focused electron probe in nanobeam EMCD mode is significantly smaller than the lateral dimensions of the individual bits (Fig. 5c), the incident beam interacts exclusively with the targeted spatial volume. Consequently, Fig. 5d, e definitively confirms that the nanobeam EMCD technique can robustly detect the reversed magnetic states of individual, closely packed bits at the deep-nanometer limit.

In this work, we have presented a fundamental physical demonstration of site-specific nanoscale patterning to overcome the superparamagnetic limit and lithographic bottlenecks at the single-bit level. By employing a Cs-corrected electron probe as a direct-pattern tool governed by real-time quantitative feedback, we have transformed the direct-patterning process from a simple observation into a controlled fabrication paradigm. This approach makes the engineering of atomically-sharp (111), (110), and (100) ferrimagnetic/antiferromagnetic interfaces a programmable parameter, thus minimizing the line-edge roughness. Our design intentionally takes advantage of exchange bias at these atomically-sharp FM/AFM interfaces to enhance magnetic stability and increase the potential areal density of information storage. By coupling our atomic precision patterning capability with in situ nanobeam EMCD, we directly verified the success of this approach. We performed the first *in-architecture* measurement of a magnetically detectable bit size of about 4 nm, which is significantly smaller than theoretical expectations for isolated bits. Crucially, by synergizing this sub-nanometer structural phase engineering with external configurational control, we successfully achieved the active writing of binary information ("1" and "0") through deterministic magnetization reversal. This comprehensive demonstration establishes a complete, closed-loop workflow—from deterministic fabrication and thermal stabilization to highly localized magnetic reading and active writing. Beyond magnetic storage, the framework presented here constitutes a general sub-nanometer fabrication primitive, providing a definitive blueprint for structural engineering at the single-lattice-site level in a wide range of quantum and semiconductor materials. While future work will need to address significant challenges in throughput and system integration, this closed-loop approach establishes a foundational pathway towards highly reliable, atomic-level precision patterning for next-generation deep-nanoscale architectures.

Methods

Sample preparation

$NiFe_2O_4$ thin films were grown on $MgAl_2O_4$ substrates using reactive radio frequency magnetron sputtering. Prior to deposition, the substrates were annealed under vacuum at 400 °C for 30 min. Following a 10-min pre-sputtering process, the nickel ferrite films were deposited at a substrate temperature of 300 °C. Cross-sectional TEM samples were prepared using an FEI Helios NanoLab 400S FIB-SEM.

STEM data collection and analysis

Atomic-resolution high-angle annular dark-field scanning transmission electron microscopy (HAADF-STEM) images were acquired at 300 kV using a JEOL ARM G2 microscope. The microscope was operated with a beam convergence semi-angle of 26 mrad and collection semi-angles ranging from 60 to 200 mrad. In a typical imaging experiment, a probe current of 11 pA and a probe size of about 56 pm were employed to observe the phase transformation in real time, enabling the acquisition of time-resolved STEM-ADF images.

To analyze the acquired image sequences, drift correction was applied to STEM-HAADF movies prior to further processing (Supplementary Movie 1). Following drift correction, the positions of Ni and Fe atomic columns, exhibiting varying coordination, were determined using atom-column indexing. Due to the four distinct occupancies observed for Fe atom columns during the phase transition, these columns were classified into four types (Site A, Site B, Site C, and Site D) (Supplementary Fig. 7b). Voronoi tessellation was performed based on the x–y coordinates of both Fe/Ni and the four types of Fe atomic columns. Each resulting Voronoi cell represented a single atomic column. Finally, the intensity of each atomic column was obtained by integrating the intensity within the corresponding Voronoi cell polygon, using the polygon as a mask on the original STEM-HAADF image.

4D-STEM data acquisition and analysis

Four-dimensional scanning transmission electron microscopy (4D-STEM) was performed at a probe current of approximately 10 pA to ensure phase stability. During each scan, a convergent beam electron diffraction (CBED) pattern was recorded at every real space pixel, yielding data cubes of 128 × 128 probe positions with 128 × 128 detector pixels per pattern. The dwell time per probe position was 13 ms. Diffraction patterns were acquired using a Gatan K3 direct electron detector, providing low-noise readout suitable for dynamic measurements.

All processing was carried out with custom Python routines. To obtain projected in-plane electric fields and iDPC images, the center of mass (COM) of every diffraction pattern was computed. The COM components along x and y (I_{comx}, I_{comy}) are proportional to the corresponding in-plane field components E_x and E_y, giving the projected field vector as $\vec{E_\perp} = E_x\vec{i} + E_y\vec{j}$. Following established formulations, the magnitude $|\vec{E_\perp}|$ is proportional to the COM shift from the geometric center, ΔCOM. For a probe with longitudinal momentum p_z and velocity υ_z traversing a specimen of thickness Δz, the projected field can be written as: $E_\perp = \Delta COM \cdot p_z \cdot \upsilon_z/(e \cdot \Delta z)$, where e is the elementary charge. The projected charge density ρ (in units of e/Å^2) was obtained by applying Gauss's law to the retrieved field: $\rho = \varepsilon_0\, \nabla \cdot E_\perp$, where ε_0 is the vacuum permittivity. The 4D-STEM simulation was performed on the Dr.Probe using the same parameters as the experiment. The extraction of iDPC and dDPC was performed using Magnifier based on the simulated 4D-STEM.

Electron beam patterning

Atomic-scale patterning of magnetic islands was performed using a JEOL ARM G2 microscope operating at 300 kV. The C_s was tuned to less than 1 μm at a convergence semi-angle of 26 mrad, achieving a spatial resolution of up to 60 picometers. The patterning process employed a probe current of 35 pA and a dwell time of 4 μs (typical dwell times range from 1 μs to 1 s), optimized for patterning efficiency and precision. Precise control over the geometry (boundary and shape) of the ferromagnetic bit was achieved by carefully aligning the electron beam's scanning direction with respect to the underlying crystallographic orientation of the sample. This technique allowed for the fabrication of bits with various shapes, including rectangles, squares, triangles, trapezoids, and parallelograms, with their boundaries aligned along specific crystallographic directions of the spinel structure ([111], [110], and [100]). By manipulating the electron beam path parameters, the spatial arrangement and dimensions of the bits were precisely controlled, enabling the creation of features with inter-bit distances as small as 3 nm and bit sizes down to 2.4 nm. A demonstration of this patterning process is provided in Supplementary Movie 2. Additionally, real-time analysis of ADF images was employed to provide immediate feedback during the fabrication process. This closed-loop control enables atomic-precision engineering of interfaces, as demonstrated in Supplementary Movie 3.

Nanobeam EMCD measurement

EELS and electron magnetic circular dichroism experiments were conducted before and after patterning on a $NiFe_2O_4$ (nickel ferrite) spinel thin film with electron beam using a 300 kV nanobeam electron microscope with channel dispersion of 0.35 eV. The microscope was configured with an energy resolution of approximately 1.1 eV, a collection semi-angle of approximately 4.9 mrad, and a convergence semi-angle of approximately 0.7 mrad. To ensure consistent analysis of specific deep nanoscale islands within the film, reference holes were milled using the electron beam. EMCD was acquired under the microscope's objective-lens field (~2.5 T) in the (004) three-beam geometry; the signal therefore represents the out-of-plane component of the magnetic moment. The signals were acquired from $NiFe_2O_4$ islands of varying size and shape by targeting the intersections of lines connecting these reference holes. To robustly extract the weak magnetic chiral dichroism signal at the deep-nanoscale limit while strictly maintaining energy resolution, nanobeam EMCD spectra were acquired using a dual-EELS frame integration method. For each targeted magnetic bit, the positive and negative chiral spectra were collected by integrating 100 individual frames with an exposure time of 0.5 s per frame. This rigorous extended integration protocol ensures an adequate signal-to-noise ratio for unambiguously determining the intrinsic local magnetic state of the sub-nanometer structured regions. EELS processing followed standard procedures: a power-law pre-edge background was subtracted, plural scattering was removed by Fourier–log deconvolution, and spectra were post-edge normalized. For normalization, the Fe L-edge "+" and "−" spectra were scaled to the integrated intensity over 730–750 eV, and the Ni L-edge "+" and "−" spectra were scaled over 880–899 eV after subtracting a step function. The thickness of samples was determined by a two-step process combining position-averaged convergent beam electron diffraction (PACBED) and EELS. In the first step, PACBED patterns were acquired along the [110] zone axis in a 300 kV aberration-corrected STEM (convergence semi-angle 26 mrad, probe current ~11 pA) and matched to multislice simulations[39]. This calibrated the inelastic mean free path $\lambda \approx 80$ nm. In the second step, λ was applied to EELS low-loss spectra, confirming $t \approx 12$ nm for the test region. The thickness of the information bits shows no significant change before and after patterning.

According to the sum rules of EMCD[40,41], for a specific system, the relative strength of EMCD defined by:

$$RS_{emcd} = \frac{5\int_{L_3}(S_+ - S_-)dE - 4\int_{L_2}(S_+ - S_-)dE}{\int_{L_3+L_2}(S_+ + S_-)dE} \quad (1)$$

is proportional to the total magnetic moment $\langle \boldsymbol{\mu} \rangle$. The RS_{emcd} is then used to evaluate the robustness of information storage.

Additionally, the orbital/spin moment ratio (m_L/m_S ratio) can be calculated, which is given by the following equation[40,41]:

$$\frac{m_L}{m_s} = \frac{2}{3}\frac{\int_{L_3}(S_+ - S_-)dE + \int_{L_2}(S_+ - S_-)dE}{\int_{L_3}(S_+ - S_-)dE - \int_{L_2}(S_+ - S_-)dE} = \frac{2q}{9p - 6q} \quad (2)$$

where q, p are the energy integrals of the MCD spectrum over both edges and the L_3 edge only, respectively.

Micromagnetic simulations

Micromagnetic simulations were conducted using the MuMax3 software package, utilizing a finite-difference discretization scheme. To accurately resolve the deep-nanoscale architectures with high spatial precision, a unit cell size of $1 \times 1 \times 1\ nm^3$ was established within a $14 \times 14 \times 12$ simulation grid. The geometric model was constructed as an embedded configuration, featuring an FM $NiFe_2O_4$ core surrounded by an AFM matrix. The lateral dimensions of the FM core were systematically varied (11, 9, 7, 5, and 3 nm) while maintaining a constant 3 nm thickness for the surrounding AFM matrix, directly reflecting the experimental boundary conditions.

To precisely capture the physical degradation of magnetic properties driven by heightened thermal fluctuations at reduced dimensions, the intrinsic material parameters for the FM core were systematically scaled as a function of the core size. Specifically, as the core dimension decreased from 11 nm to 3 nm, the saturation magnetization (M_s) was scaled from 200 kA/m to 10 kA/m, the exchange stiffness (A_{ex}) was reduced from 1.0×10^{-11} to 0.06×10^{-11} J/m, and the magnetocrystalline anisotropy constant (K_u) was lowered from 4.8 to 0.8 kJ/m^3. The Gilbert damping parameter (α) was set to 0.05.

The enclosing AFM matrix was modeled with a net zero saturation magnetization ($M_s = 0$ A/m) and a negative exchange stiffness ($A_{ex} = -1 \times 10^{-7}$ J/m) to enforce the requisite anti-parallel spin ordering. To rigorously model the interfacial pinning effect, an interfacial exchange coupling parameter was introduced at the FM/AFM boundaries. This coupling strength was scaled from 2×10^{-11} J/m for the 11 nm core down to 0.1×10^{-11} J/m for the 3 nm core, representing the increased susceptibility of the interfacial spin configuration to thermal perturbations at extreme down-scaling.

Magnetic hysteresis loops were computed by applying an external magnetic field along the z-axis, sweeping from +10 to −10 T and back to +10 T in increments of 0.2 T. At each field step, the system was allowed to reach its equilibrium state through a rigorous energy minimization protocol, utilizing a maximum torque convergence criterion of 1×10^{-5}.

Data availability

The data that support the findings of this study are available in Figshare at https://doi.org/10.6084/m9.figshare.31807078. Source data are provided with this paper.

References

1. Yuan, R. et al. Flexible memory: progress, challenges, and opportunities. *Adv. Intell. Discov.* **2**, e202500039 (2026).
2. National Academies of Sciences, Engineering, and Medicine. *Rapid Expert Consultation on Archival Data Storage Technologies for the Intelligence Community* (National Academies of Sciences, Engineering, and Medicine, 2024).
3. Lundstrom, M. S. & Alam, M. A. Moore's law: the journey ahead. *Science* **378**, 722–723 (2022).
4. Bhushan, B. Current status and outlook of magnetic data storage devices. *Microsyst. Technol.* **29**, 1529–1546 (2023).
5. Charap, S. H., Lu, P.-L. & He, Y. Thermal stability of recorded information at high densities. *IEEE Trans. Magn.* **33**, 978–983 (1997).
6. Khomutov, G. B. & Koksharov, Y. A. Organized ensembles of magnetic nanoparticles: preparation, structure, and properties. In *Magnetic Nanoparticles* (ed. Gubin, S. P.) 117–195 (Wiley-VCH, Weinheim, 2009).
7. Sbiaa, R. & Piramanayagam, S. N. Patterned media towards nano-bit magnetic recording: fabrication and challenges. *Recent Pat. Nanotechnol.* **1**, 29–40 (2007).
8. Albrecht, T. R. et al. Bit-patterned magnetic recording: theory, media fabrication, and recording performance. *IEEE Trans. Magn.* **51**, 1–42 (2015).
9. Ross, C. A. Patterned magnetic recording media. *Annu. Rev. Mater. Res.* **31**, 203–235 (2001).
10. Kikitsu, A. Prospects for bit patterned media for high-density magnetic recording. *J. Magn. Magn. Mater.* **321**, 526–530 (2009).
11. Lee, B. et al. Sub-10-nm-resolution electron-beam lithography toward very-high-density multilevel 3D nano-magnetic information devices. *J. Nanoparticle Res.* **15**, 1–8 (2013).
12. Blatt, M., Wiseman, S. & Domany, E. Superparamagnetic clustering of data. *Phys. Rev. Lett.* **76**, 3251 (1996).
13. Chen, Q. & Zhang, Z. J. Size-dependent superparamagnetic properties of $MgFe_2O_4$ spinel ferrite nanocrystallites. *Appl. Phys. Lett.* **73**, 3156–3158 (1998).

14. Liu, C. & Zhang, Z. J. Size-dependent superparamagnetic properties of Mn spinel ferrite nanoparticles synthesized from reverse micelles. *Chem. Mater.* **13**, 2092–2096 (2001).
15. Skumryev, V. et al. Beating the superparamagnetic limit with exchange bias. *Nature* **423**, 850–853 (2003).
16. Jenkins, S., Chantrell, R. W. & Evans, R. F. Exchange bias in multi-granular noncollinear $IrMn_3$/CoFe thin films. *Phys. Rev. B* **103**, 014424 (2021).
17. Dyck, O. et al. Atom-by-atom fabrication with electron beams. *Nat. Rev. Mater.* **4**, 497–507 (2019).
18. Pitters, J. et al. Atomically precise manufacturing of silicon electronics. *ACS Nano* **18**, 6766–6816 (2024).
19. Chen, I. J. et al. Precise atom manipulation through deep reinforcement learning. *Nat. Commun.* **13**, 7499 (2022).
20. Esat, T. et al. A quantum sensor for atomic-scale electric and magnetic fields. *Nat. Nanotechnol.* **19**, 1466–1471 (2024).
21. Natterer, F. D. et al. Reading and writing single-atom magnets. *Nature* **543**, 226–228 (2017).
22. Sugimoto, Y. et al. Complex patterning by vertical interchange atom manipulation using atomic force microscopy. *Science* **322**, 413–417 (2008).
23. Schmid, I. et al. Exchange bias and domain evolution at 10 nm scales. *Phys. Rev. Lett.* **105**, 197201 (2010).
24. Jiang, N. et al. Atom-by-atom fabrication by electron beam via induced phase transformations. *MRS Bull.* **42**, 653–659 (2017).
25. Klein, J. et al. Control of structure and spin texture in the van der Waals layered magnet CrSBr. *Nat. Commun.* **13**, 5420 (2022).
26. Mishra, R., Ishikawa, R., Lupini, A. R. & Pennycook, S. J. Single-atom dynamics in scanning transmission electron microscopy. *MRS Bull.* **42**, 644–652 (2017).
27. Zhang, J. et al. Interlayer reconstruction phase transition in van der Waals materials. *Nat. Mater.* **24**, 369–376 (2025).
28. Wang, Z. et al. Atomic scale imaging of magnetic circular dichroism by achromatic electron microscopy. *Nat. Mater.* **17**, 221–225 (2018).
29. Kohno, Y., Seki, T., Findlay, S. D., Ikuhara, Y. & Shibata, N. Real-space visualization of intrinsic magnetic fields of an antiferromagnet. *Nature* **602**, 234–239 (2022).
30. Gaudisson, T. et al. Polyol-made spinel ferrite nanoparticles—local structure and operating conditions: $NiFe_2O_4$ as a case study. *Front. Mater.* **8**, 668994 (2021).
31. Jiang, N. Electron beam damage in oxides: a review. *Rep. Prog. Phys.* **79**, 016501 (2015).
32. Parajuli, P. et al. Direct observation of electron beam-induced phase transition in MgCrMnO4. *Chem. Mater.* **32**, 10456–10462 (2020).
33. Frati, F., Hunault, M. O. J. Y. & de Groot, F. M. F. Oxygen K-edge X-ray Absorption Spectra. *Chem. Rev.* **120**, 4056–4110 (2020).
34. Colliex, C., Manoubi, T. & Ortiz, C. Electron-energy-loss-spectroscopy near-edge fine structures in the iron-oxygen system. *Phys. Rev. B* **44**, 11402 (1991).
35. Nellist, P. D. & Pennycook, S. J. in *Advances in Imaging and Electron Physics* Vol. 113, 147–203 (Elsevier, 2000).
36. Mitra, S., Mandal, K. & Anil Kumar, P. Temperature dependence of magnetic properties of $NiFe_2O_4$ nanoparticles embedded in SiO_2 matrix. *J. Magn. Magn. Mater.* **306**, 254–259 (2006).
37. Zhao, X., Xu, S., Wang, L., Duan, X. & Zhang, F. Exchange-biased $NiFe_2O_4$/NiO nanocomposites derived from NiFe-layered double hydroxides as a single precursor. *Nano Res.* **3**, 200–210 (2010).
38. Wang, Z. Q., Zhong, X. Y., Yu, R., Cheng, Z. Y. & Zhu, J. Quantitative experimental determination of site-specific magnetic structures by transmitted electrons. *Nat. Commun.* **4**, 1395 (2013).
39. Oberaigner, M. et al. Online thickness determination with position averaged convergent beam electron diffraction using convolutional neural networks. *Microsc. Microanal.* **29**, 427–436 (2023).
40. Calmels, L. et al. Experimental application of sum rules for electron energy loss magnetic chiral dichroism. *Phys. Rev. B Condens. Matter Mater. Phys.* **76**, 060409 (2007).
41. Rusz, J., Eriksson, O., Novák, P. & Oppeneer, P. M. Sum rules for electron energy loss near edge spectra. *Phys. Rev. B Condens. Matter Mater. Phys.* **76**, 060408 (2007).

Acknowledgements
The authors thank M. Matsumoto, Z. C. Wang, and Prof. J. Zhu for valuable discussions and contributions to this work.

Author contributions
Q.W. and X.Y.Z. conceived the research. X.Y.Z. supervised the research. Q.W. performed the experiments. D.S.H. developed the data collection method. H.Y. and E.K. fabricated the samples. Q.W. and L.J. performed the data analysis. Q.W. and X.Y.Z. wrote the initial manuscript. R.E.D.-B. and F.-R.C. revised the manuscript. All authors contributed to the final manuscript writing and approved the submission.

Funding
This work was financially supported by the National Natural Science Foundation of China (52203304), GuangDong Basic and Applied Basic Research Foundation (2024A1515012303), Science, Technology and Innovation Commission of Shenzhen Municipality (SGDX202108231 04200001), Innovation and Technology Fund (ITS/365/21), the Sino-German Mobility Programme by the Sino-German Center for Research Promotion (M-0265), the City University of Hong Kong (Projects no. 7020207, 9610484, 9680291, 9678288, 9610607) and the City University of Hong Kong Shenzhen Research Institute. The work described in this paper was substantially supported by a grant from the EU-HK Research and Innovation Cooperation Co-funding Mechanism sponsored by the Research Grants Council of Hong Kong Special Administrative Region, China (Project No. E-CityU101/20), and the Research Grants Council of the Hong Kong Special Administrative Region, China (Project No. C1013-23EF, C1018-22E, CityU 11309822, CityU 11307926). This project has received funding from the European Research Council (ERC) under the European Union's Horizon 2020 research and innovation program (Grant No. 856538, project "3D MAGiC"). This project has received funding from the Deutsche Forschungsgemeinschaft (DFG, German Research Foundation, Project No. 405553726 – TRR 270). This work made use of the resources of the TRACE TEM center at the City University of Hong Kong. This work was partly supported by the Japan Society for the Promotion of Science (JSPS) KAKENHI (23K26535).

Competing interests
The authors declare no competing interests.

Additional information
Supplementary information The online version contains supplementary material available at https://doi.org/10.1038/s41467-026-74996-9.

Correspondence and requests for materials should be addressed to Xiaoyan Zhong.

Peer review information *Nature Communications* thanks the anonymous reviewers for their contribution to the peer review of this work. A peer review file is available.

https://doi.org/10.1038/s41467-026-74996-9